Spin-Echo Mapping Spectroscopy Applied to NQR

A. P. Bussandri and M. J. Zuriaga

Facultad de Matemática Astronomia y Fisica, Universidad Nacional de Córdoba, Ciudad Universitaria, 5000 Córdoba, Argentina

A theoretical description of nuclear spin-echo Fourier-transform mapping spectroscopy (NSEFTMS) for broad NQR lines is derived from the time-domain spin-echo theory for a spin $I = \frac{3}{2}$ system. The expression found for the effective broadband RF excitation profile is similar to that in NMR spectroscopy. The main difference is the angular dependence of the nutation frequency, but this does not change the overall behavior. It is also shown that the maximum of the spin echo occurs at time $t = \tau + \frac{2}{\pi}t_{w1}$ after the second pulse, and that if the signal is acquired from this point, the phase-adjustment problem due to the off-resonance effect is avoided. A study of ^{35}Cl NQR broad lines in molecular alloys of (p-dichlorobenzene)$_{(1-x)}$ (p-dibromobenzene)$_{x}$ at different temperatures and in the incommensurate phase of bis-(4-chlorophenyl) sulfone at 77 K has been used as an example of the application of the method. The NSEFTMS method in NQR provides an efficient alternative to the time-consuming point-by-point scanning technique for the study of broad lines in solids, in particular when some sharp features exist. © 1998 Academic Press

INTRODUCTION

Nuclear quadrupole resonance (NQR) of solids is generally characterized by broad lines (in same cases hundreds of kilohertz). The line broadening is due mainly to the variation of the electric field gradient (EFG) at the site of the quadrupolar nucleus. EFG inhomogeneities arise because of the presence of dislocations, strains, impurities, lack of crystallographic order, and torsional motions of units in the crystal lattice. Incommensurate crystals (*1*), high T_c superconductors (*2*), molecular alloys (*3*), and organic glasses (*4*) are typical examples for which theoretical models have been presented for describing the NQR lineshapes.

To study extremely broad lines, one must resort to the spin-echo technique to overcome the so-called ''dead time'' problem. However, it is not possible to excite the entire broadband spectrum by a single radiofrequency (rf) pulse. Spins which are off resonance with respect to the rf pulse are poorly excited and hence their resultant signal intensities are poor. The problem of off-resonance effects could, in principle, be overcome by applying high-power rf pulses, but there are obvious technical limits to the feasibility of this approach. Moreover, as NQR signals are highly sensitive

to temperature changes, sample heating by high-power rf pulses could shift the resonance frequencies. The conventional method for circumventing this problem is, as in the NMR case, to plot the time-domain integral of the spin echo with respect to the frequency, point-by-point. But this is essentially a CW measurement and is, therefore, time consuming, especially if one wants to increase the resolution of certain spectral features.

Recently, an alternative spin-echo spectroscopy called nuclear spin-echo Fourier-transform mapping spectroscopy (NSEFTMS) has been proposed (*5*) to study broad NMR lines. The idea is that one records a series of spin echos increasing or decreasing the carrier frequency, stepwise between measurements. Then, the right half of each spin echo is Fourier transformed and phase adjusted to obtain the pure absorption spectrum. The entire spectrum is recovered by adding all individual FT spin-echo spectra. The NSEFTMS method has a subtle problem (*5*) related to the phase adjustment. This problem can be severe when the line exhibits sharp features.

A natural extension of this NMR technique is to the NQR case. Even though NQR and NMR of solids are similar techniques, they usually face diametrically opposed experimental problems (*6*). In solid-state NMR the existence of a single quantization axis provided by the external magnetic field leads to a dependence of the NMR spectrum on the relative orientation of the Zeeman and perturbing interactions (dipolar, chemical shift, and quadrupolar interactions). Exactly the opposite holds for ''pure'' or zero-field NQR. That the internal quantization axis is determined by the principal-axis system (PAS) of the EFG results in a frequency spectrum which is orientation independent. However, the rf coil introduces an external axis and thus an orientation dependence. The purpose of this paper is to present a rigorous analysis of nuclear spin-echo Fourier-transform mapping spectroscopy for broad NQR lines for spin $I = \frac{3}{2}$ nuclei.

We begin with the development of a theoretical description of spin-echo mapping in NQR using the spin-density operator formalism in the quadrupole interaction frame introduced by Pratt (*7*). Then we analyze the phase of the signal and show how to overcome the phase-adjustment procedure. To test the theory, we measured the ^{35}Cl NQR spectra of

molecular alloys of p-dichlorobenzene$_{(1-x)}$ p-dibromobenzene$_x$ (PDCB$_{(1-x)}$–PDBB$_x$) at room temperature, and at 77 K. The corresponding NQR spectra obtained by the conventional point-by-point method serve as a reliable comparison. In addition a ^{35}Cl NQR experiment was performed in the incommensurate phase of bis-(4-chlorophenyl) sulfone (BCPS) at 77 K. BCPS was chosen because at this temperature it has a line with two sharp edge singularities separated by about 300 kHz and a third rather broad intermediate peak (1). Therefore, it is a very appropriate candidate for testing the method.

THEORY

In the systems of interest the dipolar line broadening is much smaller than the inhomogeneous broadening. We seek the response of a noninteracting spin-$\frac{3}{2}$ system to a $(t_{w_{(1)}})_{\varphi_{(1)}} - \tau - (t_{w_{(2)}})_{\varphi_{(2)}}$ excitation sequence involving two rf pulses of durations $t_{w_{(1)}}$ and $t_{w_{(2)}}$ with phases $\varphi_{(1)}$ and $\varphi_{(2)}$, respectively. Phase cycling could be necessary since the echo produced can be corrupted by the FID of the second pulse and even by remnants of the FID due to the first pulse (8).

The Hamiltonian for an ensemble of noninteracting spin-$\frac{3}{2}$ nuclei experiencing electric quadrupole coupling and in the presence of an rf field is given by

$$H_T(t) = H_Q + H_{rf}(t). \qquad [1]$$

The quadrupolar and rf Hamiltonian may be written as (7, 9)

$$H_Q = \frac{1}{2} \sum_{j=1}^{N} \omega_{Qj} Q_j \qquad [2]$$

and

$$H_{rf}(t) = \gamma H_1 \cos(\omega_{rf} t + \varphi) \sum_{j=1}^{N} (I_{xj} \sin \theta_j \cos \phi_j$$
$$+ I_{yj} \sin \theta_j \sin \phi_j + I_{zj} \cos \theta_j), \qquad [3]$$

where ω_{Qj} and Q_j are the resonance frequency and the quadrupolar operator (9) at the site of spin j, respectively. The orientation of the PAS at the site of spin j relative to the rf coil axis is given by Euler angles θ_j and ϕ_j. The density-operator formalism introduced by Pratt (7) will be used to follow the evolution of the spin system in the quadrupole interaction frame (QIF) defined by the operator $U(t) = \exp[i(\omega_{rf}/2)Qt]$ with $Q = \Sigma_j Q_j$. The time-independent part of the transformed total Hamiltonian in the QIF has the form

$$\tilde{H}_T = \tilde{H}_Q + \tilde{H}_{rf} \qquad [4]$$

with

$$\tilde{H}_Q = \sum_{j=1}^{N} \frac{1}{2} \Delta\omega_{Qj} Q_j = \sum_{j=1}^{N} \tilde{h}_{Qj} \qquad [5]$$

$$\tilde{H}_{rf}(\varphi) = \sum_{j=1}^{N} \frac{1}{2} \omega_1 (A_j \cos \varphi + B_j \sin \varphi) = \sum_{j=1}^{N} \tilde{h}_{rfj}, \qquad [6]$$

where $\Delta\omega_{Qj} = \omega_{Qj} - \omega_{rf}$ defines the offset frequency and $\omega_1 = \gamma H_1$. The single-spin operators A_j and B_j which depend on (θ_j, ϕ_j) are identical to those given by Pratt (7).

The reduced thermal equilibrium density matrix, $\rho(0)$, is expressed as (10)

$$\rho(0) = C H_Q = \sum_{j=1}^{N} \frac{C}{2} \omega_{Qj} Q_j = \sum_{j=1}^{N} \rho_j(0). \qquad [7]$$

The evolution of the density matrix in the QIF and after the second pulse of the spin-echo sequence can be expressed as

$$\rho^*(t) = \sum_{j=1}^{N} \rho_j^*(t) = \sum_{j=1}^{N} T_j(t) \rho_j(0) T_j(t)^{-1} \qquad [8]$$

with

$$T_j(t) = T_{0j}(t) R_{j(2)}(t_{w_{(2)}}, \varphi_{(2)}) T_{0j}(\tau) R_{j(1)}(t_{w_{(1)}}, \varphi_{(1)}), \qquad [9]$$

where t is measured from the end of the second pulse. $R_j(t_w, \varphi)$ is the time-evolution operator during the application of the rf pulses; it includes effects of $\tilde{h}_{Qj}$ and $\tilde{h}_{rfj}(\varphi)$. $T_{0j}(t)$ is the free-evolution operator governed only by $\tilde{h}_{Qj}$.

The experimentally observed signal, $S(t)$, will be proportional to the time-varying expectation value of the total spin component, I_T, resolved along the rf coil axis, where (7, 9)

$$I_{Tcoil}^* = \sum_{j=1}^{N} A_j \cos \omega t - B_j \sin \omega t + C_j \qquad [10]$$

$$S(t) = \langle I_{Tcoil}^*(t) \rangle = \sum_{j=1}^{N} \text{Tr}[\rho_j^*(t)(A_j \cos \omega t$$
$$- B_j \sin \omega t + C_j)] = \sum_{j=1}^{N} S_j(t, \Delta\omega_{Qj}, \theta_j, \phi_j).$$
$$[11]$$

Now S_j is the contribution to the signal from the jth nucleus with a particular orientation of the EFG given by (θ_j, ϕ_j).

In a straightforward, but tedious, process, the commutation properties of the operators Q_j, A_j, and B_j (7) can be used to calculate the evolution of Q_j, A_j, and B_j under the influence of $R(t_w, \varphi)$ and $T_0(t)$. These transformations are

given in Appendix I. Using these results, the density matrix given in Eq. [8] can be written

$$\rho_j^*(t) = \frac{C_j'}{2}\omega_{Qj}Q_j + \rho_{j(1\,\text{Fid})}^*(t+\tau)$$

$$+ \rho_{j(2\,\text{Fid})}^*(t) + \rho_{j(\text{Echo})}^*(t-\tau). \qquad [12]$$

In this expression the first term does not contribute to the signal, the second term corresponds to the FID following the first pulse, the third term is due to the FID after the second pulse, and the fourth term corresponds to the echo signal. The expressions for each component are given in Appendix II.

With $\rho_j^*(t)$ given above, the induced signal S_j (Eq. [11]) is calculated to be

$$S_j(t, \Delta\omega_{Qj}, \theta_j, \phi_j) = S_{j(1\,\text{Fid})}e^{i\Delta\omega_{Qj}(t+\tau)}e^{i\varphi_{(1)}}$$

$$+ S_{j(2\,\text{Fid})}e^{i\Delta\omega_{Qj}t}e^{i\varphi_{(2)}} + S_{j(\text{Echo})}e^{i\Delta\omega_{Qj}(t-\tau)}e^{i(2\varphi_{(2)}-\varphi_{(1)})}, \quad [13]$$

where $S_{j(1\,\text{Fid})}$, $S_{j(2\,\text{Fid})}$, and $S_{j(\text{Echo})}$ are the complex amplitudes and they do not depend on the pulse phase, φ. From this equation it is clear that coaddition of signals resulting from four-step phase cycling, $\varphi_{(1)} = 0, 180°, 0, 180°$ and $\varphi_{(2)} = 0, 90°, 180°, 270°$, would result in the selection of only the echo component. This phase cycle is similar to that employed in NMR spectroscopy (11). It is valid for arbitrary (θ, ϕ) values, and therefore for polycrystalline samples. The same phase cycle was derived using a tensor-operator formalism for the particular case $t_{w_{(1)}} = t_{w_{(2)}}$, $\Delta\omega_{Qj} = 0$, and for orientation $\theta = \frac{\pi}{2}$, $\phi = 0$ of the PAS with respect to the rf coil axis. Using these values the expression obtained by Sunitha et al. (8) for the amplitude of the signal is reproduced in Eqs. [AII.4], [AII.5], and [AII.6].

The complex amplitude for the spin-echo signal is given by

$$S_{j(\text{Echo})} = C\omega_{Qj}\lambda_j^2\xi_{j(2)}(-\epsilon_{j(1)} + i\alpha_{j(1)}) = S_{B_j} + iS_{A_j},$$

where

$$S_{B_j}(\Delta\omega_{Qj}, \omega_1, \theta_j, \phi_j) = -C\omega_{Qj}\lambda_j^4\frac{\omega_1^3}{\omega_{ej}^3}\sin(\omega_{ej}t_{w_{(1)}})$$

$$\times [1 - \cos(\omega_{ej}t_{w_{(2)}})] \quad [14]$$

$$S_{A_j}(\Delta\omega_{Qi}, \omega_1, \theta_j, \phi_j) = C\omega_{Qj}\lambda_j^4\frac{\Delta\omega_{Qj}\omega_1^3}{\omega_{ej}^4}$$

$$\times [1 - \cos(\omega_{ej}t_{w_{(1)}})][1 - \cos(\omega_{ej}t_{w_{(2)}})]. \quad [15]$$

The complex amplitudes for the FID signals due to the first and second pulse are given in Appendix II.

Assuming that there is no correlation between ω_{Qj} and θ_j, ϕ_j, it is possible to simplify Eq. [11] by introducing the quadrupolar frequency distribution $g(\omega)$. The result is

$$S(t, \theta, \phi) = \int_{-\infty}^{\infty} g(\omega')S(t, \omega' - \omega_{\text{rf}}, \theta, \phi)$$

$$\times e^{i(\omega'-\omega_{\text{rf}})(t-\tau)}d\omega'$$

$$= \int_{-\infty}^{\infty} [S_{AB}e^{i\vartheta}]e^{i(\omega'-\omega_{\text{rf}})(t-\tau)}d\omega', \qquad [16]$$

where

$$S_{AB}(\omega - \omega_{\text{rf}}, \omega_1, \theta, \phi) = g(\omega)(S_A^2 + S_B^2)^{1/2} \quad [17]$$

$$\vartheta(\omega - \omega_{\text{rf}}, \omega_1, \theta, \phi) = \arctan\frac{S_A}{S_B}. \qquad [18]$$

The physical picture described by Eq. [16] is as follows. For a given set of parameters $t_{w_{(1)}}$, $t_{w_{(2)}}$, $\Delta\omega$, and ω_1, the projection of the magnetization on the plane defined by A and B after two pulses gives an absorption component S_B in the B direction, and a dispersion component S_A in the A direction. The equations for S_B and S_A (Eq. [14] and Eq. [15]) are similar to those found for NMR spectroscopy, except for the angular dependence of λ. S_{AB} is the pure absorption spectrum, and if $g(\omega)$ is a slowly varying function of ω, then S_{AB} basically reflects the power spectrum of the rf pulse:

$$p_S = (S_B^2 + S_A^2)^{1/2}. \qquad [19]$$

The response of a polycrystalline specimen is obtained by considering an average over all orientations,

$$\langle S(t)\rangle = \frac{1}{4\pi}\int_{\Omega} S(t, \theta, \phi)d\Omega$$

$$= \int_{-\infty}^{\infty} \langle S_{AB}\rangle e^{i\langle\vartheta\rangle}e^{i(\omega'-\omega_{\text{rf}})(t-\tau)}d\omega', \qquad [20]$$

where $\langle S_{AB}\rangle = g(\omega)(\langle S_A\rangle^2 + \langle S_B\rangle^2)^{1/2}$ and $\langle\vartheta\rangle = \arctan(\langle S_A\rangle/\langle S_B\rangle)$.

We have used a computer simulation to obtain p_S (Eq. [19]) and ϑ (Eq. [18]) as a function of the offset parameter $\Delta\omega/\omega_1$ for single crystals with $\eta = 0$, and for powder samples with $\eta = 0$ and $\eta = 1$. The width of the first pulse t_{w1} and frequency ω_1 were set such that $\frac{\sqrt{3}}{2}\omega_1 t_{w_{(1)}} = \frac{\pi}{2}$ and $t_{w_{(2)}} = 2t_{w_{(1)}}$. This represents the usual $(\pi/2)_0 - \tau - (\pi)_0$ spin-echo experimental conditions for a single crystal with $\theta =$
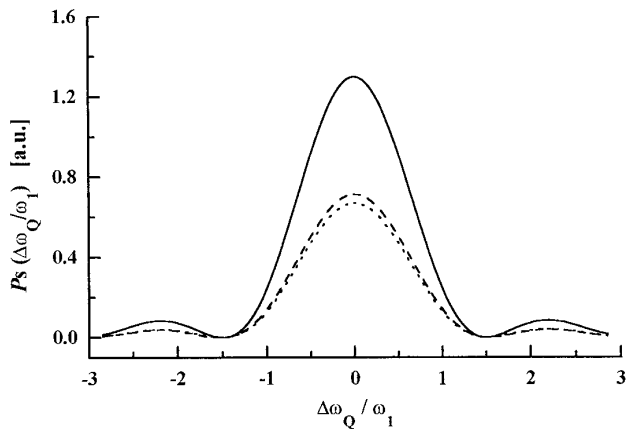
FIG. 1. Plot of the rf pulse spectrum $p(\Delta\omega/\omega_1)$ (Eq. [19]) for different cases. The solid line corresponds to $p(\Delta\omega/\omega_1)$ calculated for a single crystal; the dashed and dotted lines are for powder samples with $\eta = 1$ and $\eta = 0$, respectively.

90° and $\phi = 0°$. The results are shown in Fig. 1 and Fig. 2, respectively.

It is clear from Fig. 1 that the primary difference between single crystals and powders with arbitrary η is a deterioration of the magnetization. The reason is that quadrupolar nuclei for which the z axis of the EFG is oriented along the coil axis do not contribute to the signal. The first pair of nodes of the rf power spectrum p_S appear at $\Delta\omega = \pm 1.5\omega_1$. Within this region, as shown in Fig. 2, the phase ϑ varies almost linearly with $\Delta\omega/\omega_1$ in the three cases analyzed. The first discontinuities of ϑ also occur at approximately $\Delta\omega = \pm 1.5\omega_1$. A pure absorption spectrum can be obtained in this region by the conventional phase-adjustment procedure. However, the behavior of ϑ allows us to find a simple relationship between phase and frequency offset. From Eq. [18] it follows that, for a single crystal with $\eta = 0$ and $\frac{\sqrt{3}}{2}\omega_1 t_{w_{(1)}} = \frac{\pi}{2}$, the phase ϑ has the form

$$\vartheta(x) = \arctan\left[\frac{x}{(x^2 + 1)^{1/2}} \tan\left(\frac{\pi}{4}(x^2 + 1)^{1/2}\right)\right] \quad [21]$$

with $x = (2/\sqrt{3})(\Delta\omega_Q/\omega_1)$. It is easily seen that this result can be approximated by $\vartheta(x) = -x$. Therefore, the dependence of the phase in single crystals as well as in powders with arbitrary η is well represented by

$$\langle\vartheta(\Delta\omega/\omega_1)\rangle \simeq -\frac{2}{\sqrt{3}}\frac{\Delta\omega}{\omega_1} = -\frac{2}{\pi}t_{w_{(1)}}\Delta\omega. \quad [22]$$

This approximation is shown in Fig. 2; it is valid up to $\Delta\omega_Q \simeq \pm 1.36\omega_1$. Substituting Eq. [22] into Eq. [20] we have

$$\langle S(t)\rangle = \int_{-\infty}^{\infty}\langle S_{AB}\rangle e^{i(\omega'-\omega_{rf})(t-\tau-2/\pi t_{w_{(1)}})}d\omega'. \quad [23]$$

This shows that the maximum of the echo occurs for $t = \tau + \frac{2}{\pi}t_{w_{(1)}}$ as in the NMR case (12). Even though this result is exact only for the case of single crystals with $\eta = 0$, $\theta = 90°$, and $\phi = 0°$, it has been confirmed experimentally, within the limit of the digitalization (0.5 μs), for all the measured spin echos. Acquiring the echo from this time on and performing the Fourier transform of $\langle S(t')\rangle$ we obtain the pure absorption spectrum

$$F(\omega, \omega_{rf}) = 2\pi g(\omega)(\langle S_B\rangle^2 + \langle S_A\rangle^2)^{1/2}$$
$$= 2\pi g(\omega)\langle p_S\rangle \quad [24]$$

within the region $\Delta\omega = \pm 1.36\omega_1$, *with no need of phase adjustment.*

If the linewidth $\delta\omega$ of $g(\omega)$ is much smaller than ω_1, then for the region where $g(\omega)$ is different from zero the power spectrum is constant. In these situations

$$F(\omega, \omega_{rf}) = \text{cte } g(\omega). \quad [25]$$

This is exactly the same result as for FT NQR spectroscopy of narrow lines.

If $\delta\omega \gg \omega_1$, the pulse sequence can excite only those nuclei which resonate at a frequency near the carrier frequency ω_{rf}. *Spin-echo mapping spectroscopy* in NQR can therefore be formulated as in NMR, defining the function (choosing the center of the entire mapped spectrum as the origin)
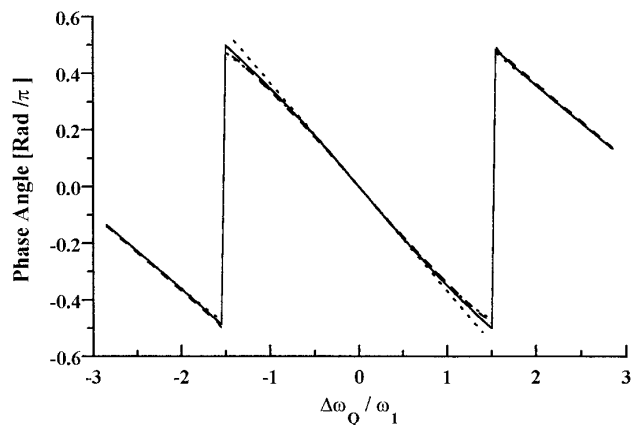

FIG. 2. Dependence of the signal phase φ on the offset $\Delta\omega/\omega_1$. Solid lines were calculated for a single crystal using Eq. [21]. Dotted and dot–dashed lines correspond to powder samples with $\eta = 0$ and $\eta = 1$, respectively. The dashed line was calculated using the linear approximation given by Eq. [22].

$$G(\omega) = \sum_{n=-N}^{N} F(\omega, \omega_{rf} = n\Lambda)$$

$$= 2\pi g(\omega) \sum_{n=-N}^{N} \langle p_S(\omega - n\Lambda, \omega_1) \rangle$$

$$= 2\pi g(\omega) P(\omega), \qquad [26]$$

where $2N + 1$ is the number of spectra recorded, and Λ is the mapping step. As mentioned above (see Eq. [24]) $F(\omega, n\Lambda)$ already represents the pure absorption spectrum for the region $|\omega - n\Lambda| \leq 1.36\omega_1$. Retaining only the central part of p_S within this range, Eq. [26] may be written as

$$G(\omega) = 2\pi g(\omega) \sum_{n=-N}^{N} \langle p_S(\omega - n\Lambda, \omega_1) \rangle$$

$$= 2\pi g(\omega) P(\omega) \qquad [27]$$

with

$$\langle p_S(\omega - n\Lambda, \omega_1) \rangle = 0 \quad \text{for } |\omega - n\Lambda| \geq 1.36\omega_1. \quad [28]$$

For $G(\omega)$ to trace precisely $g(\omega)$, $P(\omega)$ should be constant within the region of interest. We have calculated the function $P(\omega)$ with different mapping steps and different relations between ω_1 and $t_{w_{(2)}}$. In NQR the relation between the flip angle and the duration of the applied pulse varies with the asymmetry parameter, η (7). In Fig. 3 we show the results for $P(\omega)$ mapping about 0.6 MHz. For the mapping step $\Lambda \leq \omega_1$, $P(\omega)$ is approximately constant within the mapping region in a similar manner to NMR. The figure also illustrates that by working with low power, or short pulses, oscillations may be avoided. Therefore under conditions which are not very difficult to optimize in practice, the mapped spectrum $G(\omega)$ records exactly the same spectral features as $g(\omega)$.

For $\omega = \omega_{rf}$, Eq. [24] gives

$$F(\omega_{rf}) = 2\pi g(\omega_{rf}) \langle \lambda \sin(\lambda \omega_1 t_{w_{(1)}}) [1 - \cos(\lambda \omega_1 t_{w_{(2)}})] \rangle.$$

$$[29]$$

This relation can be used to trace out $g(\omega)$ point-by-point in the same manner as the conventional method.

EXPERIMENTAL RESULTS

In this section we will describe the experimental procedure and present some experimental results to test the procedure developed above. The ^{35}Cl NQR experiments were carried out using an automated, homemade NQR spectrometer with quadrature detection. The conventional Hahn echo sequence, $(\pi/2)_0 - \tau - (\pi)_0$, was used to record the spectra. The τ value
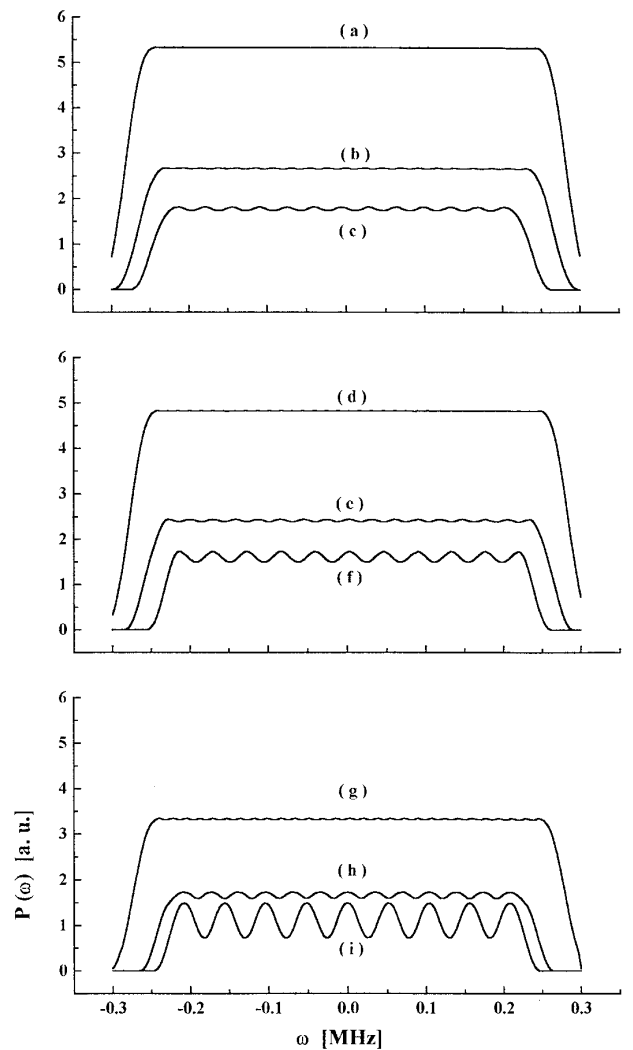

FIG. 3. Plot of the function $P(\omega)$ with the window filtering defined in Eq. [28] and with different mapping step (Λ) and pulse width $t_{w_{(2)}}$: (a–c) $\frac{\sqrt{3}}{2}\omega_1 t_{w2} = 0.8\,\pi$ and $\Lambda = 0.5\omega_1$, ω_1, and $1.5\omega_1$, respectively. (d–f) $\frac{\sqrt{3}}{2}\omega_1 t_{w2} = \pi$ and $\Lambda = 0.5\omega_1$, ω_1, and $1.5\omega_1$, respectively. (g–i) $\frac{\sqrt{3}}{2}\omega_1 t_{w2} = 1.2\pi$ and $\Lambda = 0.5\omega_1$, ω_1, and $1.5\omega_1$, respectively.

was set such that $\tau \gg T_2^*$ in order to eliminate distortions from the FIDs due to the pulses.

To obtain the mapped spectrum, we first recorded a set of spin echoes, decreasing the carrier frequency by a series of constant steps over the region of the signal. These spin echoes were then Fourier transformed and added. The mapping step was chosen so that it could be obtained by simply shifting an integral number of spectral points. To determine ω_1, we first performed a π-pulse calibration to determine the pulse width, t_w, which gave zero signal for the ^{35}Cl NQR narrow line in pure p-dichlorobenzene ($\delta\nu < 1$ kHz). It is known (13) that for a powder this occurs when $\frac{\sqrt{3}}{2}\omega_1 t_w = 1.155\,\pi$.
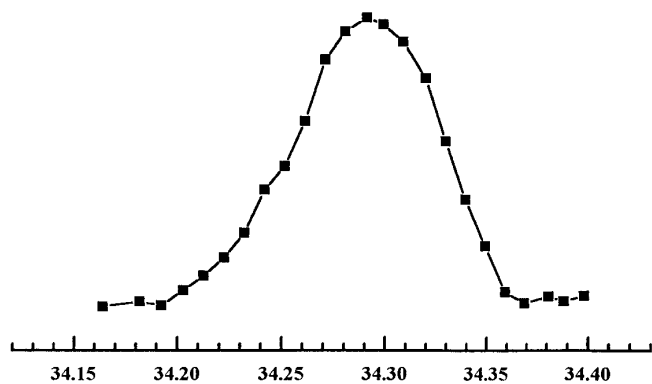
FIG. 4. Room-temperature ^{35}Cl NQR spectra in molecular alloys of PDCB$_{70}$–PDBB$_{30}$ obtained by the spin-echo point-by-point method.

FIG. 6. ^{35}Cl NQR spectra in molecular alloys of PDCB$_{(1-x)}$–PDBB$_x$ with $x = 0.1$ and $x = 0.3$ at 77 K. The presence of two lines and their relative intensities are in agreement with the model developed in Ref. (3).

Molecular alloy of PDCB$_{(1-x)}$–PDBB$_{(x)}$. The $\pi/2$ pulse width used was 15 μs which corresponds to a value for ν_1 = $\omega_1/2\pi$ of about 22 kHz. The value of τ was set to 80 μs and the number of scans was 400. The acquisition time for each spin echo was 512 μs. The mapping step was 11.696 kHz ($\simeq 0.5\nu_1$) which represent a six-point shift. We show for comparison, Fig. 4, the ^{35}Cl NQR spectrum obtained with the spin-echo point-by-point method. In the region $\delta \simeq 4\nu_1$ around the peak, the spectrum is almost symmetric and can be relatively well represented by a Gaussian function with $\sigma \simeq 22$ kHz. Thus, a single FT spectrum recorded in this region by means of a spin echo should reproduce the characteristics of the theoretical spectrum given by Eq. [24] with $g(\omega) = \exp(-(\omega - \omega_0)^2/2\sigma^2)$. This is confirmed in Fig. 5a where we have plotted theoretical and experimental spin-echo FT spectra. In Fig. 5b we present the mapped spectrum
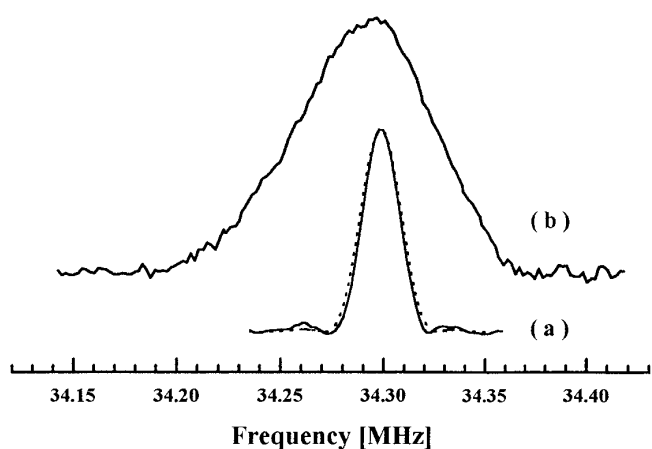
formulated from Eq. [26] and Eq. [28]. One can clearly see that Fig. 5b reproduces faithfully the whole spectrum, as expected from the theory. NQR spectra of two molecular alloys were obtained at 77 K and they are shown in Fig. 6. The relative intensities of the two peaks observed in each spectrum are in accord with the theoretical model (3).

Bis-(4-chorophenyl) sulfone (BCPS). The $\pi/2$ pulse length in this case was 10 μs which gives $\nu_1 = 33$ kHz. The acquisition time for each spin echo was 512 μs. The mapping step was 27.343 kHz ($\simeq 0.8\nu_1$) which represents a 14-point shift. The value of τ was set to 300 μs and the number of scans was 400. Figure 7 shows the 10 individual spectra necessary for mapping the full spectrum. The overall lineshape is in very good agreement with that shown in Ref. (1), as determined point-by-point with about 100 points. Therefore, for an equal number of scans the time consumed is reduced by a factor of 10, due to the fact that each point of each subspectra provides information about the lineshapes. It is worth noting that in Fig. 7a the nodes in all the subspectras are separated from their respective peaks by approximately 1.36 ν_1 as predicted by the theory.

CONCLUSIONS

We have shown theoretically that, under typical conditions for spin-echo experiments to study broad NQR lines, spin-echo mapping spectroscopy can precisely reproduce the NQR spectrum with arbitrary linewidth by choosing a suitable constant mapping step in a manner analogous to NMR. We have seen that the maximum of the spin echo occurs at $t = \tau + \frac{2}{\pi}t_{w_{(1)}}$ after the second pulse, either for narrow or for broad lines. By acquiring the signal from the top of the echo, no phase-adjustment procedure is required. The experimental results confirm this theoretical prediction. This result is most important when the line has sharp features

FIG. 5. (a) ^{35}Cl NQR spectra of single spin-echo FT spectrum in PDCB$_{70}$–PDBB$_{30}$ with the carrier frequency set at the peak of the line. The experimental data (solid line) are superimposed with the spectrum obtained from Eq. [17] (dotted line) where the pure NQR line $g(\omega)$ was assumed with a root-mean-squared deviation of 22 kHz. (b) The mapped spectra by NSEMFTS formulated by Eq. [26] and Eq. [28].
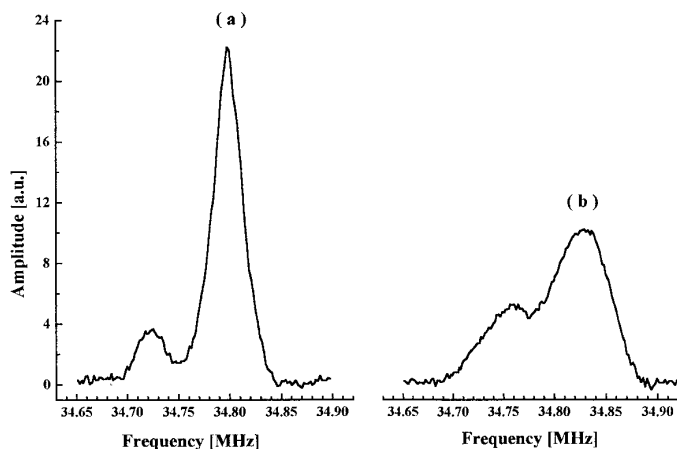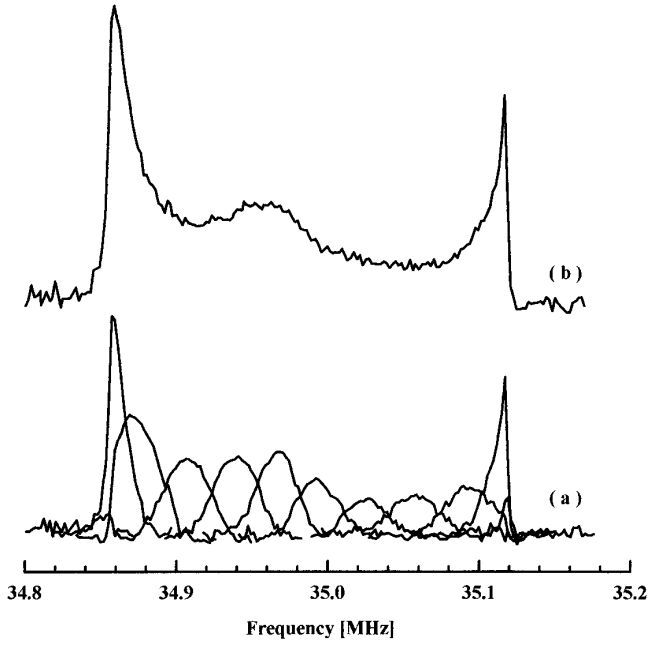
because the manual phase-adjustment procedure is time consuming. Spin-echo mapping spectroscopy has certain advantages over the conventional point-by-point method, the most important of which is the reduction in the time required to obtain the spectrum, especially when it has sharp features.

It is important to notice that if there is a correlation between ω_{Qj} and the orientation of the PAS given by (θ_j, ϕ_j), the assumptions that allow one to obtain Eq. [16] and Eq. [20] are not valid. Such correlations exist in the same incommensurate system, but not for BCPS (*14*) where the incommensurate distortion consists of a modulation of the dihedral angle between the benzene rings and the Cl–S–Cl plane which preserves the direction of the PAS.

Finally, one might note that by using the evolution of the operators Q_j, A_j, and B_j given in Appendix I one can calculate the response of a quadrupolar-spin ensemble to a multiple-pulse excitation sequence with rf pulses of arbitrary duration and phase.

APPENDIX I

The transformation properties of the Q, A, and B operators under $T_0(t)$ and $R(t_w, \varphi)$ are as follows:

$$T_{0j}(t) = e^{-i\tilde{h}_{Qj}t}; \quad R_j(t_w, \varphi) = e^{-i(\tilde{h}_{Qj} + \tilde{h}_{rfj}(\varphi))t_w}$$

$$T_{0j}A_j T_{0j}^{-1} = A_j\cos(\Delta\omega_{Qj}t) + B_j\sin(\Delta\omega_{Qj}t) \quad \text{[AI.1]}$$

$$T_{0j}B_j T_{0j}^{-1} = -A_j\sin(\Delta\omega_{Qj}t) + B_j\cos(\Delta\omega_{Qj}t) \quad \text{[AI.2]}$$

$$R_j Q_j R_j^{-1} = (\alpha_j\cos\varphi + \epsilon_j\sin\varphi)A_j$$
$$+ (\alpha_j\sin\varphi - \epsilon_j\cos\varphi)B_j + \gamma_j Q_j \quad \text{[AI.3]}$$

$$R_j A_j R_j^{-1} = \chi_j A_j + \kappa_j B_j - \xi_j\sin\varphi(A_j\sin\varphi - B_j\cos\varphi)$$
$$+ \lambda_j^2(-\epsilon_j\sin\varphi + \alpha_j\cos\varphi)Q_j \quad \text{[AI.4]}$$

$$R_j B_j R_j^{-1} = -\kappa_j A_j + \chi_j B_j$$
$$+ \xi_j\cos\varphi(A_j\sin\varphi - B_j\cos\varphi)$$
$$+ \lambda_j^2(\epsilon_j\cos\varphi + \alpha_j\sin\varphi)Q_j \quad \text{[AI.5]}$$

$$\gamma_j = \frac{\Delta\omega_{Qj}^2}{\omega_{ej}^2} + \frac{\lambda_j^2\omega_1^2}{\omega_{ej}^2}\cos(\omega_{ej}t_w); \quad \epsilon_j = \frac{\omega_1}{\omega_{ej}}\sin(\omega_{ej}t_w);$$

$$\alpha_j = \frac{\omega_1\Delta\omega_{Qj}}{\omega_{ej}^2}[1 - \cos(\omega_{ej}t_w)]$$

$$\chi_j = \frac{\Delta\omega_{Qj}^2}{\omega_{ej}^2}\cos(\omega_{ej}t_w) + \frac{\lambda_j^2\omega_1^2}{\omega_{ej}^2}; \quad \kappa_j = \frac{\Delta\omega_{Qj}}{\omega_{ej}}\sin(\omega_{ej}t_w);$$

$$\xi_j = \frac{\lambda_j^2\omega_1^2}{\omega_{ej}^2}[1 - \cos(\omega_{ej}t_w)]$$

$$\omega_{ej} = \sqrt{\Delta\omega_{Qj}^2 + \lambda_j^2\omega_1^2}$$

$$\lambda_j(\theta_j, \phi_j) = \frac{\sqrt{3}}{2a}\sin\theta_j\left[1 + \eta\frac{2}{3}\cos(2\phi_j)\right.$$
$$\left. + \eta^2\frac{(1 + 4\cot^2\theta_j)}{9}\right]^{1/2}$$

$$a = \sqrt{1 + \frac{\eta^2}{3}},$$

where η is the asymmetry parameter of the EFG.

APPENDIX II

The terms of the density matrix appearing in Eq. [12] are as follows (the subscripts (1) and (2) indicate that the coefficients refer to pulses (1) and (2), respectively):

$$C_j' = C\{\gamma_{j_{(1)}}\gamma_{j_{(2)}} + \lambda_j^2[(\alpha_{j_{(1)}}\epsilon_{j_{(2)}} + \alpha_{j_{(2)}}\epsilon_{j_{(1)}})$$
$$\times \sin(\Delta\omega_{Qj}\tau + \varphi_{(1)} - \varphi_{(2)})$$
$$+ (\alpha_{j_{(1)}}\alpha_{j_{(2)}} - \epsilon_{j_{(1)}}\epsilon_{j_{(2)}})$$
$$\times \cos(\Delta\omega_{Qj}\tau + \varphi_{(1)} - \varphi_{(2)})]\} \quad \text{[AII.1]}$$

$$\rho_{j_{(1\,\text{Fid})}}^*(t + \tau) = \frac{C}{4}\omega_{Qj}\{A_j[(\alpha_{j_{(1)}}(2\chi_{j_{(2)}} - \xi_{j_{(2)}})$$
$$+ 2\epsilon_{j_{(1)}}\kappa_{j_{(2)}})\cos(\Delta\omega_{Qj}(t + \tau) + \varphi_{(1)})$$
$$+ (\epsilon_{j_{(1)}}(2\chi_{j_{(2)}} - \xi_{j_{(2)}}) - 2\alpha_{j_{(1)}}\kappa_{j_{(2)}})$$
$$\times \sin(\Delta\omega_{Qj}(t + \tau) + \varphi_{(1)})]$$

$$+ B_j[-(\epsilon_{j_{(1)}}(2\chi_{j_{(2)}} - \xi_{j_{(2)}}) - 2\alpha_{j_{(1)}}\kappa_{j_{(2)}})$$

$$\times \cos(\Delta\omega_{Qj}(t + \tau) + \varphi_{(1)})$$

$$+ (\alpha_{j_{(1)}}(2\chi_{j_{(2)}} - \xi_{j_{(2)}}) + 2\epsilon_{j_{(1)}}\kappa_{j_{(2)}})$$

$$\times \sin(\Delta\omega_{Qj}(t + \tau) + \varphi_{(1)})]\} \qquad [\text{AII.2}]$$

$$\rho^*_{j_{(2\,\text{Fid})}}(t) = \frac{C}{2}\,\omega_{Qj}\gamma_{j_{(1)}}\{A_j[\alpha_{j_{(2)}}\cos(\Delta\omega_{Qj}t + \varphi_{(2)})$$

$$+ \epsilon_{j_{(2)}}\sin(\Delta\omega_{Qj}t + \varphi_{(2)})]$$

$$+ B_j[-\epsilon_{j_{(2)}}\cos(\Delta\omega_{Qj}t + \varphi_{(2)})$$

$$+ \alpha_{j_{(2)}}\sin(\Delta\omega_{Qj}t + \varphi_{(2)})]\} \qquad [\text{AII.3}]$$

$$\rho^*_{j_{(\text{Echo})}}(t - \tau) = \frac{C}{4}\,\omega_{Qj}\xi_{j_{(2)}}\{A_j[\alpha_{j_{(1)}}\cos(\Delta\omega_{Qj}(t - \tau)$$

$$+ 2\varphi_{(2)} - \varphi_{(1)}) - \epsilon_{j_{(1)}}\sin(\Delta\omega_{Qj}(t - \tau)$$

$$+ 2\varphi_{(2)} - \varphi_{(1)})] + B_j[\epsilon_{j_{(1)}}\cos(\Delta\omega_{Qj}(t - \tau)$$

$$+ 2\varphi_{(2)} - \varphi_{(1)}) + \alpha_{j_{(1)}}\sin(\Delta\omega_{Qj}(t - \tau)$$

$$+ 2\varphi_{(2)} - \varphi_{(1)})]\}. \qquad [\text{AII.4}]$$

The complex amplitudes in Eq. [13], as calculated from Eq. [11], are given by

$$S_{j_{(1\,\text{Fid})}} = C\omega_{Qj}\lambda_j^2((\epsilon_{j_{(1)}}(2\chi_{j_{(2)}} - \xi_{j_{(2)}}) - 2\alpha_{j_{(1)}}\kappa_{j_{(2)}})$$

$$+ i(\alpha_{j_{(1)}}(2\chi_{j_{(2)}} - \xi_{j_{(2)}}) + 2\epsilon_{j_{(1)}}\kappa_{j_{(2)}}))$$

$$= C\omega_{Qj}\lambda_j^2\,\frac{\omega_1}{\omega_{ej}^3}\,\{-2\Delta\omega_{Qj}^2[\sin(\omega_{ej}t_{w_{(2)}})$$

$$- \sin(\omega_{ej}(t_{w_{(1)}} + t_{w_{(2)}}))] + \lambda_j^2\omega_1^2\sin(\omega_{ej}t_{w_{(1)}})$$

$$\times [1 + \cos(\omega_{ej}t_{w_{(2)}})] + i\,\frac{\Delta\omega_{Qj}}{\omega_{ej}}$$

$$\times \{(\omega_{ej}^2 + \Delta\omega_{Qj}^2)\cos(\omega_{ej}(t_{w_{(2)}} + t_{w_{(1)}}))$$

$$+ 2\Delta\omega_{Qj}^2\cos(\omega_{ej}t_{w_{(2)}})$$

$$+ \lambda_j^2\omega_1^2[-1 + \cos(\omega_{ej}t_{w_{(2)}}) - \cos(\omega_{ej}t_{w_{(1)}})$$

$$+ \sin(\omega_{ej}t_{w_{(1)}})\sin(\omega_{ej}t_{w_{(2)}})]\}\} \qquad [\text{AII.5}]$$

$$S_{j_{(2\,\text{Fid})}} = C\omega_{Qj}\lambda_j^2\xi_{j_{(2)}}(\epsilon_{j_{(2)}} + i\alpha_{j_{(2)}})$$

$$= \frac{C\omega_{Qj}2\lambda_j^2\omega_1}{\omega_{ej}^3}(\Delta\omega_{Qj}^2 + \lambda_j^2\omega_1^2\cos(\omega_{ej}t_{w_{(2)}}))$$

$$\times \left\{\sin(\omega_{ej}t_{w_{(2)}}) + i\,\frac{\Delta\omega_{Qj}}{\omega_{ej}}[1 - \cos(\omega_{ej}t_{w_{(2)}})]\right\}$$

$$[\text{AII.6}]$$

$$S_{j_{(\text{Echo})}} = C\omega_{Qj}\lambda_j^2\xi_{j_{(2)}}(-\epsilon_{j_{(1)}} + i\alpha_{j_{(1)}})$$

$$= \frac{C\omega_{Qj}\lambda_j^4\omega_1^3}{\omega_{ej}^3}[1 - \cos(\omega_{ej}t_{w_{(1)}})]\left\{-\sin(\omega_{ej}t_{w_{(1)}})\right.$$

$$\left. + i\,\frac{\Delta\omega_{Qj}}{\omega_{ej}}[1 - \cos(\omega_{ej}t_{w_{(1)}})]\right\}. \qquad [\text{AII.7}]$$

ACKNOWLEDGMENTS

REFERENCES

1. U. Mikac, T. Apih, J. Dolinsek, J. Seliger, J. Slak, and R. Blinc, *Phys. Rev. B* **54,** 9141 (1996).
2. T. Shimizu *et al., J. Phys. Soc. Jpn.* **57,** 2494 (1988).
3. I. M. Alymov, G. K. Semin, T. L. Khotsyanova, and T. A. Babushkina, *Izv. Akad. Nauk SSR, Ser. Fiz.* **39,** 2457 (1975).
4. A. E. Wolfenson, A. H. Brunetti, D. J. Pusiol, and W. M. Pontuschka, *Phys. Rev. B* **41,** 6257 (1990).
5. Y. Tong, *J. Magn. Reson. A* **119,** 22 (1996).
6. G. S. Harbison and A. Slokenbrgs, *J. Chem. Phys.* **90,** 5292 (1989).
7. J. C. Pratt, *Mol. Phys.* **34,** 539 (1977).
8. N. Sunitha Bai, N. Reddy, and R. Ramachandran, *J. Magn. Reson. A* **102,** 137 (1993).
9. S. Su and R. Armstrong, *J. Magn. Reson. A* **101,** 265 (1993).
10. M. A. Singh and R. L. Armstrong, *Phys. Rev. B* **38,** 50 (1988).
11. D. L. Turner, *Prog. NMR Spectrosc.* **17,** 281 (1985).
12. C. P. Slichter, ''Principles of Magnetic Resonance,'' 3rd ed., Springer-Verlag, New York (1990).
13. M. Goldman, *Adv. Magn. Reson.* **14,** 59 (1990).
14. J. Etrillard, J. Even, M. Sougoti, P. Launois, S. Longeville, and B. Toudic, *Solid State Commun.* **87,** 47 (1993).